AGU PUBLICATIONS

JGR

Journal of Geophysical Research: Space Physics

RESEARCH ARTICLE
10.1002/2017JA024209

Key Points:
- Multispacecraft observations and 3-D global hybrid simulations are used to investigate the ion temperature gradient in the Earth's magnetotail
- Temperature profiles used to reconstruct plasma and magnetic field properties in the entire magnetotail
- Theoretical approaches used to incorporate the ion temperature gradient into kinetic current sheet models

Correspondence to:
S. Lu,
slu@igpp.ucla.edu

Citation:
Lu, S., A. V. Artemyev, V. Angelopoulos, Y. Lin, and X. Y. Wang (2017), The ion temperature gradient: An intrinsic property of Earth's magnetotail, *J. Geophys. Res. Space Physics*, *122*, 8295–8309, doi:10.1002/2017JA024209.

Received 30 MAR 2017
Accepted 24 JUL 2017
Accepted article online 26 JUL 2017
Published online 10 AUG 2017

The ion temperature gradient: An intrinsic property of Earth's magnetotail

San Lu[1], A. V. Artemyev[1,2], V. Angelopoulos[1], Y. Lin[3], and X. Y. Wang[3]

[1]Department of Earth, Planetary, and Space Sciences and Institute of Geophysics and Planetary Physics, University of California, Los Angeles, California, USA, [2]Space Research Institute, RAS, Moscow, Russia, [3]Department of Physics, Auburn University, Auburn, Alabama, USA

Abstract Although the ion temperature gradient along (X_{GSM}) and across (Z_{GSM}) the Earth's magnetotail, which plays a key role in generating the cross-tail current and establishing pressure balance with the lobes, has been extensively observed by spacecraft, the mechanism responsible for its formation is still unknown. We use multispacecraft observations and three-dimensional (3-D) global hybrid simulations to reveal this mechanism. Using THEMIS (Time History of Events and Macroscale Interactions during Substorms), Geotail, and ARTEMIS (Acceleration, Reconnection, Turbulence and Electrodynamics of Moon's Interaction with the Sun) observations during individual, near-simultaneous plasma sheet crossings from 10 to 60 R_E, we demonstrate that the ion temperature Z_{GSM} profile is bell-shaped at different geocentric distances. This Z_{GSM} profile is also prevalent in statistics of ~200 THEMIS current sheet crossings in the near-Earth region. Using 3-D global hybrid simulations, we show that mapping of the X_{GSM} gradient of ion temperature along magnetic field lines produces such a bell-shaped profile. The ion temperature mapping along magnetic field lines in the magnetotail enables construction of two-dimensional distributions of these quantities from vertical (north-south) spacecraft crossings. Our findings suggest that the ion temperature gradient is an intrinsic property of the magnetotail that should be considered in kinetic descriptions of the magnetotail current sheet. Toward this goal, we use theoretical approaches to incorporate the temperature gradient into kinetic current sheet models, making them more realistic.

1. Introduction

The global picture of plasma convection in the Earth's magnetosphere assumes earthward motion of charged particles from the distant tail region, where shocked magnetosheath particles enter the magnetosphere [*Dungey*, 1963]. Dominated by E × B drift in the dawn-dusk electric field E_y, this motion results in particle heating [*Lyons*, 1984; *Ashour-Abdalla et al.*, 1994] and establishes a temperature profile from the distant tail (where ion energies are about 1 keV) [*Zwickl et al.*, 1984; *Slavin et al.*, 1985] to the near-Earth tail (where ion energies are higher than 10 keV) [*Wang et al.*, 2004; *Kissinger et al.*, 2012]. Similar temperature increase along the earthward direction was inferred from the ionosphere [*Wing and Newell*, 1998, 2002; *Wing et al.*, 2014]. This plasma temperature's earthward increase (together with a density increase) provides an earthward plasma pressure gradient that balances magnetic field tension forces, as illustrated in most existing magnetotail models (see review by *Schindler* [2006], and references therein).

As well observed by spacecraft, this plasma temperature nonuniformity exists not only along the tail (in the GSM *x* direction) but also in the GSM *y* (dawn-dusk) and *z* (across the tail) directions. The dawn-dusk temperature gradient forms in the near-Earth region and can be attributed to curvature and gradient duskward drifts of hot ions [*Wang et al.*, 2006; *Wing and Newell*, 1998, 2002; *Guild et al.*, 2008; *Lu et al.*, 2016a]. Regarding the temperature nonuniformity in the GSM *z* direction, the first Geotail results in the distant tail showed that the ion temperature (T_i) has a distinct bell-shaped profile in the north-south direction across the tail [*Hoshino et al.*, 1996]: T_i plotted versus B_x—a proxy of distance from the neutral sheet—has a parabolic shape, with a maximum at the neutral plane, where $B_x = 0$. Further investigations using Cluster data showed that the gradient $\partial T_i/\partial B_x$ is also strong in the near-Earth tail current sheet [*Runov et al.*, 2006; *Artemyev et al.*, 2011]. This gradient contributes more significantly to the pressure balance in the magnetotail along the *z* direction than the density gradient [*Runov et al.*, 2006].

To better understand two-dimensional (2-D) nonuniform plasma temperature profiles in the *x*-*z* plane in the magnetotail, a key question needs to be addressed: What is the relationship between the *x* gradient and the *z*

gradient of plasma temperature? An appropriate approach to doing so is to use a global hybrid simulation model [e.g., *Lin et al.*, 2014; *Lu et al.*, 2015a, 2015b, 2016a] that describes (1) ion convection motion in a global scale from the lunar distance to the near-Earth plasma sheet edge and (2) small-scale ion kinetics, which is important to resolve ion isotropization caused by scattering within the magnetotail current sheet [*Ashour-Abdalla et al.*, 1994; *Kaufmann et al.*, 2002]. In this study we combine multispacecraft observations with 3-D global hybrid simulations to explain how the bell-shaped $T_i(B_x)$ profile across the tail is formed and how it relates to the earthward ion temperature (T_i) increase. The multispacecraft observations are presented in section 2, and the 3-D global hybrid simulations are presented in section 3.

Comparing the temperature $T_i(B_x)$ profiles from our hybrid simulations to spacecraft observations provides an additional opportunity to probe distant tail plasma and magnetic field properties using vertical current sheet crossing by spacecraft. And, indeed, fast magnetotail oscillations [e.g., *Sergeev et al.*, 2006] or current sheet thinning [e.g., *Artemyev et al.*, 2016a] often brought spacecraft to the boundary of the magnetotail current sheet, where they measured a cold ion population. If simulations can connect these cold ions with the ion population in the distant tail, such spacecraft measurements at the current sheet boundary can be used to probe downtail conditions. We explore this idea in section 4.

Because the ion temperature gradient is an intrinsic property of the magnetotail current sheet, one should take it into account in current sheet investigations. In most previous kinetic models of the magnetotail current sheet, however, the plasma temperature is still assumed to be uniform along and across the tail (therefore, in these models, the plasma pressure gradient is assumed to be contributed by the plasma density gradient, not the temperature gradient) [e.g., *Schindler and Birn*, 2002; *Birn et al.*, 2004; *Yoon and Lui*, 2005]. An important exception is the one-dimensional (1-D) thin current sheet model proposed by *Sitnov et al.* [2000, 2006] and *Zelenyi et al.* [2000, 2011] in which a finite population of Speiser ions [*Speiser*, 1965] supports the plasma temperature z gradient. Generalization of such 1-D models to two dimensions in the x-z plane, however, has just begun [*Sitnov and Merkin*, 2016]. No further investigations of plasma temperature distributions in the thin current sheet have been done. To advance in this direction, in section 5 we consider theoretical approaches which allow including such nonuniform temperature profiles in kinetic current sheet models.

2. Multispacecraft Observations

We consider two data sets of spacecraft observations to demonstrate that bell-shaped $T_i(B_x)$ profiles form simultaneously at different distances from the Earth and represent a ubiquitous property of the magnetotail configuration. We start this section with a description of data sets and methods and then present our results from spacecraft observations.

2.1. Data and Methods

For near-simultaneous investigations of the magnetotail at different geocentric distances, we use several events from the data set collected in *Artemyev et al.* [2017]. This data set includes events during which Time History of Events and Macroscale Interactions during Substorms (THEMIS) D, Geotail, and Advanced Relay and Technology Mission (ARTEMIS) P1 (THEMIS B) visited the magnetotail plasma sheet within 2 days. Each event consists of several crossings of the magnetotail current sheet by all spacecraft. In the current sheet crossings, we used the magnetic field component B_x as a proxy of the satellite distance to the neutral plane ($B_x = 0$): a higher $|B_x|$ means a larger distance to the neutral plane (although the relation is not linear). The magnetic field was measured by fluxgate magnetometers on board THEMIS/ARTEMIS [*Auster et al.*, 2008] and by the magnetic field experiment on board Geotail [*Kokubun et al.*, 1994]. Because the pressure/temperature anisotropy in the magnetotail is weak and almost unmeasurable [e.g., *Stiles et al.*, 1978; *Wang et al.*, 2013], we use the isotropic ion temperature T_i measured by the electrostatic analyzer (ESA) on board ARTEMIS [*McFadden et al.*, 2008] and by the low-energy particles (LEP) experiment on board Geotail [*Mukai et al.*, 1994]. To cover the contribution of high-energy ions to T_i at the near-Earth magnetotail, we use combined measurements of ESA and solid state telescope (SST) on board THEMIS D [*Angelopoulos*, 2008]. Figures 1a–1c show three sets of spacecraft orbits for events when THEMIS D, Geotail, and ARTEMIS P1 probed the magnetotail current sheet within few days. THEMIS D (and THEMIS E, with the very close orbit to THEMIS D) crosses the midnight magnetotail around $x \approx -10\ R_E$; Geotail approaches the midnight

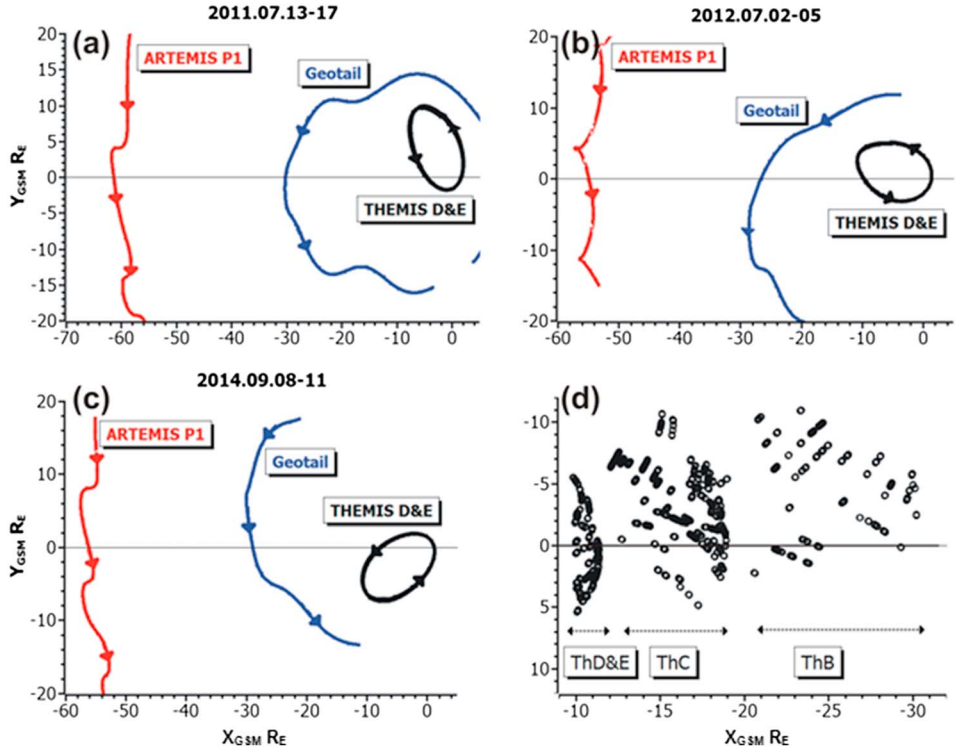

Figure 1. (a–c) Three sets of THEMIS/Geotail/ARTEMIS X_{GSM}-Y_{GSM} orbits correspond to the three events shown in Figure 2. (d) Distribution of current sheet crossings, in the X_{GSM}-Y_{GSM} plane, observed by THEMIS spacecraft in 2009, which corresponds to the statistics shown in Figure 3.

magnetotail around $x \approx -30\ R_E$; and ARTEMIS P1 crosses the magnetotail current sheet around the lunar orbit $x \approx -55\ R_E$.

The spacecraft (THEMIS/Geotail/ARTEMIS) crossed the magnetotail current sheet because of magnetotail flapping oscillations. Therefore, the duration of the current sheet crossing and corresponding T_i measurements differs for different flapping velocities. To obtain a representative $T_i(B_x)$ profile for each event, we separate the B_x range into bins and calculate the average T_i for each bin during the current sheet crossing.

Ion temperature measurements at different geocentric distances by THEMIS D, Geotail, and ARTEMIS P1 provide a global picture of the magnetotail T_i distribution for several events. To obtain a statistical result, we consider 200 current sheet crossings by THEMIS E, THEMIS D, THEMIS B, and THEMIS C in 2009. Although all five THEMIS spacecraft were operating in the magnetotail, THEMIS A was located too close to the Earth and usually did not probe the magnetotail current sheet. THEMIS E and THEMIS D had very similar trajectories; their current sheet crossings provided almost identical T_i profiles; and they were probing the current sheet mostly at $x \in [-12, -9]\ R_E$; THEMIS C and THEMIS B were probing current sheet mostly at $x \in [-14, -30]\ R_E$. Figure 1d shows the current sheet crossing distribution in the equatorial (x-y) plane from our data set. We use ESA data for THEMIS C and THEMIS B and combined ESA and SST data for THEMIS D to measure ion temperature.

The near-Earth magnetotail (as observed by THEMIS D and THEMIS E at $x \approx -10\ R_E$) is rather stable; it rarely experiences flapping motion strong enough that equatorially orbiting THEMIS spacecraft can encounter the boundary of the current sheet (which is at about $B_x \approx 40$ nT at this distance). During current sheet thinning, however, such observations are indeed possible [e.g., *Artemyev et al.*, 2016a]. We use one such event when three THEMIS spacecraft (D, E, and A) observed current sheet thinning for 1 h at midnight and simultaneously ARTEMIS P1 observed a flapping current sheet at midnight, $x \approx -58\ R_E$. This event from the *Artemyev et al.* [2016a] data set allows us to test our simulation results regarding the connection between ion populations measured at the boundary of the near-Earth tail and in equatorial downtail region (section 4).

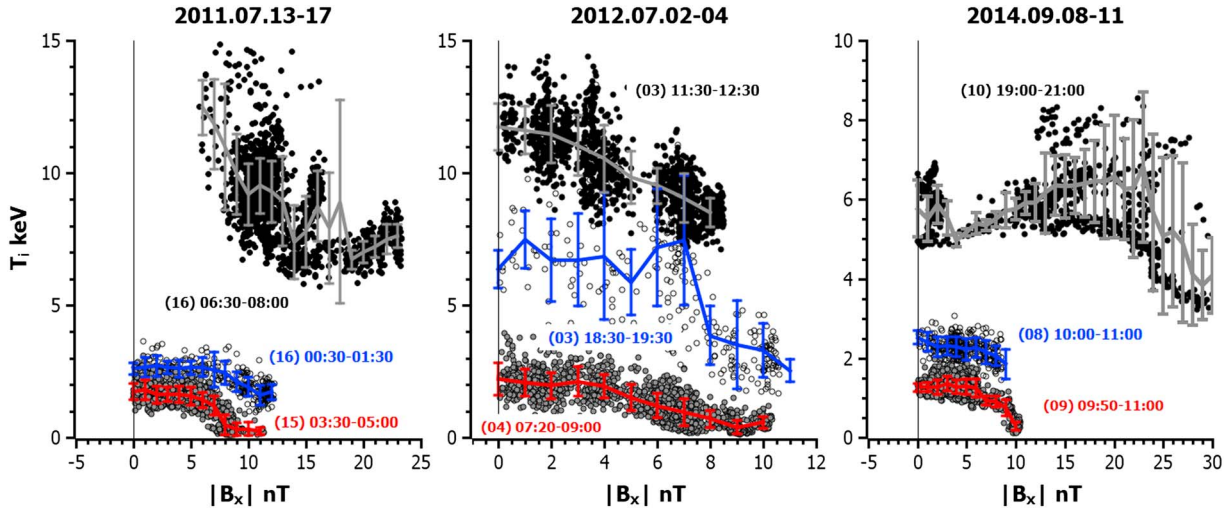

Figure 2. Ion temperature T_i(keV) versus magnetic field $|B_x|$(nT), black and grey circles indicate measured data, and colored curves with errors show averaged data: THEMIS D at $x \approx -10R_E$, (grey curve, filled black circles), Geotail at $x \approx -25R_E$ (blue curve, empty black circles), and ARTEMIS P1 at $x \approx -55R_E$ (red curve, filled grey circles). For each averaged profile, we show day (in brackets) and time interval of measurements.

2.2. Temperature $T_i(B_x)$ Profiles

Figure 2 shows three events of THEMIS D, Geotail, and ARTEMIS P1 observations of $T_i(B_x)$ at different distances from the Earth. THEMIS D crossed the current sheet at $x \approx -10$ R_E; Geotail crossed the current sheet at $x \approx -25$ R_E; and ARTEMIS P1 crossed the current sheet around lunar orbit $x \approx -55$ R_E (see also Figures 1a–1c). All three spacecraft collected sets of T_i at different distances from the neutral plane (i.e., at different B_x). We plot in Figure 2 T_i versus $|B_x|$ to show measurements at $B_x < 0$ with those at $B_x > 0$. Clearly, T_i decreases when $|B_x|$ increases, i.e., spacecraft observe colder ions at the current sheet boundary than near its center (the neutral sheet). Averaged $T_i(B_x)$ profiles shown in Figure 2 look self-similar at different geocentric distances, $x \approx -10$ R_E, -25 R_E, and -55 R_E (i.e., renormalization of T_i, $|B_x|$ peak values should collapse all three profiles observed by the three spacecraft into one). The $T_i(B_x)$ profiles show that the T_i decreases away from the neutral plane toward the current sheet boundaries is a universal property of the magnetotail current sheet, independent of geocentric distance.

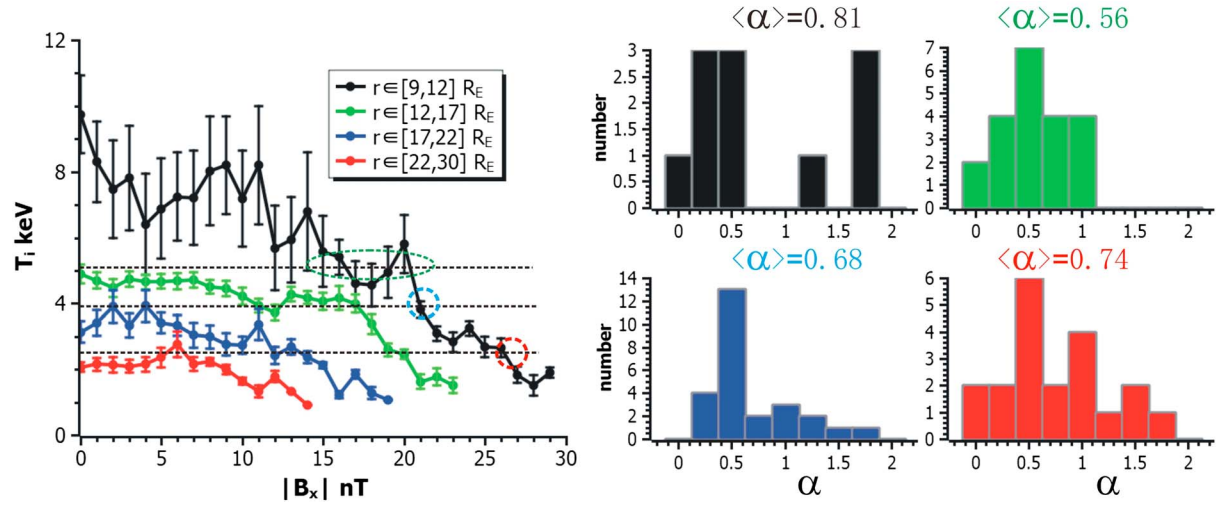

Figure 3. (left) Averaged profiles of ion temperature for THEMIS statistics of current sheet crossings in 2009. Dashed lines show the peak values of ion temperature for three profiles and corresponding values at the profile collected close to the Earth. (right) Distribution of the fitting parameter α for current sheets collected at three radial distances.

Using the current sheet crossing data set shown in Figure 1d, we plot four averaged $T_i(B_x)$ profiles in Figure 3. Each consists of more than 10 $T_i(B_x)$ profiles collected from individual current sheet crossings. Therefore, the presented data are statistically representative. The largest plasma earthward temperature gradient is observed between $x \approx -15\ R_E$ and $x \approx -10\ R_E$ [see also, *Kissinger et al.*, 2012; *Artemyev et al.*, 2016b]. Comparing Figures 2 and 3, one can see that the $T_i(B_x)$ profiles with a peak at $B_x = 0$ exist in both individual crossings at $x \in [-10, -55]\ R_E$ and in data statistics at $x \in [-10, -30]\ R_E$.

To characterize $T_i(B_x)$ profiles, we approximate them with a bell-shaped fit $T_i = T_0[1 - \alpha(B_x/B_0)^2]$, where T_0 is the ion temperature at $B_x = 0$ and B_0 is the magnetic field magnitude at the current sheet boundary [*Artemyev et al.*, 2011, 2017]. We obtain B_0 from the vertical pressure balance, $B_0 = \left(\left\langle B_x^2 + B_y^2 + 2\mu_0 p_i \right\rangle\right)^{1/2}$, where the averaging is performed over the entire time interval of the current sheet crossing, and p_i is the ion thermal pressure. The fitting parameter α defines the gradient of the ion temperature across the current sheet; when α is larger, the gradient in the z direction is also larger. Figure 3 shows distributions of α for four radial distances. Except for $x \approx -10\ R_E$, where statistics is not large enough, the α distributions peak at around $\alpha \approx 0.5$, and have a long tail of large α values. For $x \in [-30, -15]\ R_E$, we perceive a trend: larger α corresponds to the more distant tail.

3. Three-Dimensional Global Hybrid Simulations

Figures 2 and 3 show that the bell-shaped $T_i(B_x)$ profiles are an intrinsic property of the magnetotail as observed by multispacecraft. These observations, however, cannot explain how such temperature profiles are formed in the magnetotail. To address this question, we use a 3-D global hybrid simulation of the Earth's magnetosphere.

3.1. Simulation Model

Our 3-D global hybrid simulation model is AuburN Global hybrid codE in 3-D (ANGIE3D) (see detailed descriptions in *Lin et al.* [2014, 2017]). In hybrid simulations, ions are treated as particles and electrons are assumed to be a massless fluid. The simulation is performed in a cubic box in GSM coordinates. The simulation domain is $-60\ R_E \le x \le 20\ R_E$ and $-30\ R_E \le y, z \le 30\ R_E$. The initial condition is a dipole magnetic field plus a mirror dipole at $x < 15\ R_E$ and uniform solar wind and interplanetary magnetic field (IMF) at $x > 15\ R_E$. The procedure of imposing a mirror dipole field ensures a divergence-free transition from the constant IMF to the Earth's dipole field, which is common in many global-scale simulation models of the Earth's magnetosphere with solar wind and IMF [e.g., *Raeder et al.*, 1995; *Karimabadi et al.*, 2014]. In this study, we use solar wind velocity $V_{SW} = -700$km/s along the $-x$ direction, solar wind density $n_{SW} = 6\text{cm}^{-3}$, and temperature $T_{iSW} = 10$ eV. The IMF is purely southward $B_{IMF} = (0, 0, -10)$ nT. In our simulation we use nonuniform Cartesian grids with a high resolution, $\Delta x = \Delta y = \Delta z = 0.15\ R_E$, in the near-tail region, and the grid size is larger at the other regions, like distant tail. Distant tail has a lower density, thus a larger ion inertial length; therefore, it is safe to use a larger grid size in the distant tail with ion inertial scale still resolved there. A total of $N_x \times N_y \times N_z = 373 \times 217 \times 217$ grids and more than 3×10^9 particles are employed. The main time step for push particles is $dt = 0.05\Omega_i^{-1}$ (Ω_i based on B_{IMF}). Electromagnetic fields are updated with subcycling time steps. Ten subcycling steps make up one main step. A cold, incompressible ion fluid assumption is used for the inner magnetosphere with $r < 6\ R_E$. The subcycling time scheme for the electromagnetic field update and the cold ion approximation for the inner magnetosphere are enormously economical with computer resources. The dayside boundary at $x = 20\ R_E$ is a fixed boundary acting as a stationary source of solar wind and IMF. The other five boundaries of the simulation box are open. The inner boundary is at $r = 3.5\ R_E$, where particles are reflected and a magnetospheric-ionospheric (ionosphere located at $r = 1.08\ R_E$) electrostatic model is employed to regulate the electromagnetic fields at the inner boundary [e.g., *Raeder et al.*, 1995]. For simplicity, we adopt a uniform Pedersen conductance $\Sigma_P = 5$ S, and the Hall conductance is set to zero.

3.2. Simulation Results

In the 3-D global hybrid simulation, the magnetosphere is formed self-consistently by interaction between the solar wind and the geomagnetic field. Well-developed bow shock, magnetosheath, magnetopause, and magnetotail configurations are obtained gradually, especially after $t = 800$ s (for more details, see *Lu*

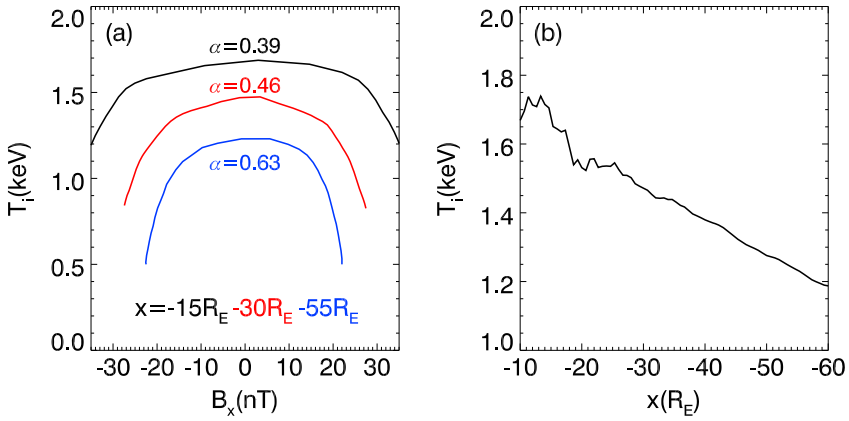

Figure 4. Ion temperature profiles from the 3-D global hybrid simulation at $t = 1430$ s. (a) Ion temperature profiles $T_i(B_x)$ at $x = -15\ R_E$ (black), $-30\ R_E$ (red), and $-55\ R_E$ (blue) averaged over $-10\ R_E \le y \le 10\ R_E$. (b) Ion temperature $T_i(x)$ profiles in the equatorial plane ($z = 0$), also averaged over $-10\ R_E \le y \le 10\ R_E$.

et al. [2016a]). Figure 4a shows ion temperature $T_i(B_x)$ profiles at different x locations ($x = -15, -30, -55\ R_E$) at $t = 1430$ s. At each x location, all the $T_i(B_x)$ profiles have a bell-shaped feature. For example, at $x = -30\ R_E$, the ion temperature is about 1.5 keV near the neutral plane and is much lower at the current sheet boundaries, about 0.8 keV. Note that the ion temperature is higher at $x = -15\ R_E$ and lower at $x = -30\ R_E$ and $-55\ R_E$. Figure 4b shows more clearly the ion temperature (at the equatorial plane around $B_x = 0$) earthward increase from 1.2 keV at $x = -60\ R_E$ to 1.7 keV at $x = -10\ R_E$. We also use the parabolic function, $T_i = T_0[1 - \alpha(B_x/B_0)^2]$, to fit the $T_i(B_x)$ profiles from the simulation. The values of the parameter α derived from the simulation (see Figure 4) are within the range $\alpha \in [0.3, 0.7]$, and α decreases with the distance to the Earth. Observations shown in Figure 3 demonstrate that α values collected for current sheet statistics have a non-Gaussian distributions, but a significant population of observed current sheets is characterized by $\alpha \in [0.25, 0.75]$. Therefore, the ranges of α values derived from simulations and observations are similar.

Figure 4 shows that the ion temperature has both x gradient and z gradient (indicated by the bell-shaped $T_i(B_x)$ profiles) in the magnetotail. In Figure 5 the 2-D ion temperature distribution in the x-z plane is plotted. Ions in the magnetotail current sheet are moving/bouncing along magnetic field lines, especially during quiet time (without ongoing explosive phenomena). To correlate the x gradient and z gradient of the ion temperature, Figure 6a plots the field-aligned gradient of ion temperature $\nabla_{\parallel} T_i$ which is shown to be small (much smaller than the ion temperature z gradient $\nabla_z T_i$ which is also plotted, see Figure 6b for comparison) and negligible in the magnetotail. Therefore, in the absence of $\nabla_{\parallel} T_i$, the vertical $T_i(B_x)$ profile can be considered as a direct mapping of $T_i(x)$ along the magnetic field lines (note that an assumption of $\nabla_{\parallel} T_i \approx 0$ is also used for mapping temperature along the field line from the ionosphere to the plasma sheet [see *Wing and Newell*,

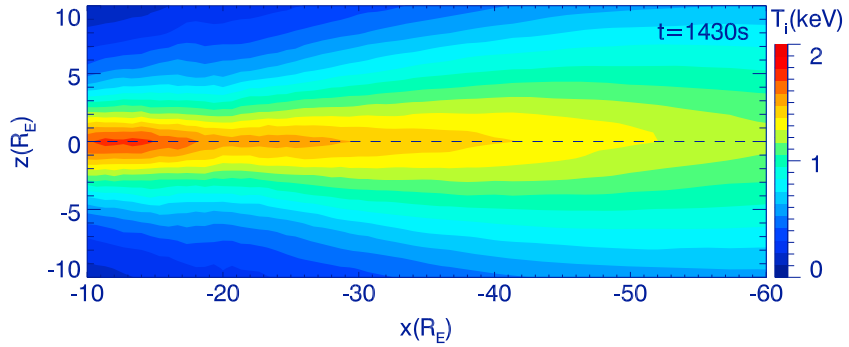

Figure 5. Ion temperature distribution in the x-z plane averaged over $-10\ R_E \le y \le 10\ R_E$ at $t = 1430$ s.

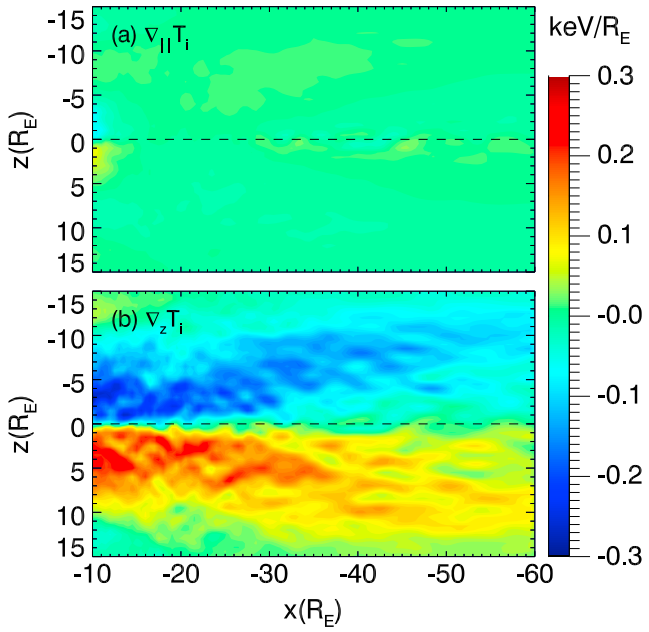

Figure 6. Ion temperature (a) field-aligned gradient $\nabla_{\|} T_i$ and (b) z gradient $\nabla_z T_i$ in the noon-midnight meridian plane ($y = 0$) at $t = 1430$ s. The temperature gradients are in units of keV/R_E.

1998, 2002]). For example, as shown in Figure 5, at $x = -10$ R_E, the ion temperature at $z = \pm 1$ R_E is mapped from $x \approx -35$ R_E in the equatorial plane ($z = 0$), and the ion temperature at $z = \pm 2$ R_E is lower and mapped from farther downtail ($x \approx -50$ R_E) in the equatorial plane. The ion temperature's x gradient (T_i increases from the tail toward the Earth) results from ion heating during earthward convection [*Lyons*, 1984; *Ashour-Abdalla et al.*, 1994]. Thus, colder ions from the downtail region move/bounce along the magnetic field lines and bring their lower temperature to higher $|B_x|$ locations.

Figure 7 shows the temporal evolution of the ion temperature at $(x, y, z) = (-10, 0, 0)$ R_E. At $t = 1430$ s, the temperature profile is already bell shaped, with $\alpha = 0.32$, because of the temperature mapping along the magnetic field lines in absence of field-aligned gradient of ion temperature. At $t = 2023$ s after reconnection and its resultant structures (e.g., dipolarization fronts and bursty bulk flows) start to form in the near-Earth region, the bell-shaped profile becomes more pronounced (α increases to 0.53) because the central current sheet is heated by reconnection [e.g., *Drake et al.*, 2009; *Hietala et al.*, 2015; *Lu et al.*, 2016b] and earthward moving flux tubes (in observations usually referred to dipolarization fronts and/or bursty bulk flows) [e.g., *Artemyev et al.*, 2012; *Birn et al.*, 2013; *Lin et al.*, 2017], whereas the current sheet's upper and lower boundaries are filled by cold plasmas moving along the magnetic field lines from the distant tail. After this, the magnetotail becomes more and more dynamic, with more and more reconnection, dipolarization fronts, and bursty bulk flows formed (for more details of the ANGIE3D simulation results of reconnection and its resultant structures, see *Lin et al.* [2014, 2017] and *Lu et al.* [2015a], *Lu et al.*, 2015b]), causing more and more ions to be energized in the magnetotail and injected into the near-Earth region. At $t = 2488$s, the current sheet is further heated to about 4 keV, and the bell-shape parameter α further increases to 0.68. The boundaries of the current sheet are also significantly heated from $t = 2023$ s to $t = 2488$ s.

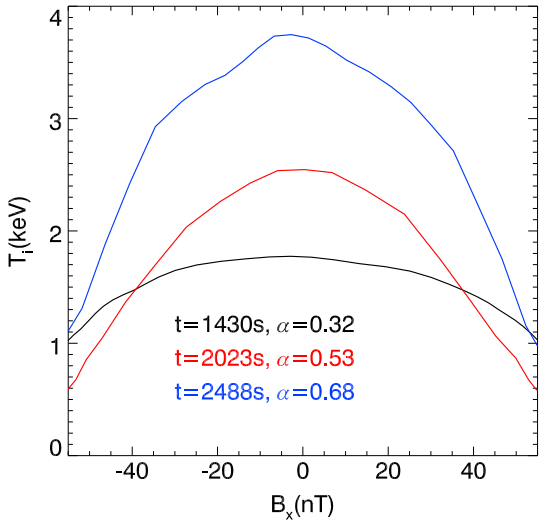

Figure 7. Ion temperature $T_i(B_x)$ profiles at $(x, y, z) = (-10, 0, 0)$ R_E at three different times, $t = 1430$ s (black), $t = 2023$ s (red), and $t = 2488$ s (blue).

The ion temperature observed by the spacecraft at $x \approx -10$ R_E is about 5–10 keV (see Figure 2 and *Artemyev et al.* [2017]), whereas the ion temperature in the hybrid simulations reaches only $T_i \approx 2$ keV in the near-Earth tail (see Figure 4). Because

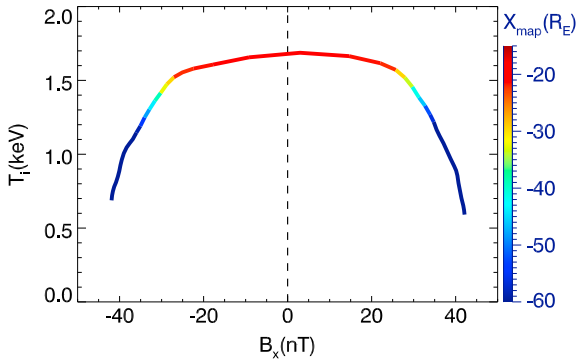

Figure 8. Ion temperature profiles $T_i(B_x)$ at $x = -15\ R_E$ from Figure 4a. The color indicates the mapping distance x_{map} of the corresponding location in the equatorial plane.

reconnection complicates the magnetotail geometry (the aforementioned formation of dipolarization fronts and bursty bulk flows/flux tubes, which can further heat the ions), we plotted spatial profiles before the first reconnection in the magnetotail begins. As a result, the magnetotail ions in the simulation are rather cold (colder than the observed ions). As the simulation proceeds, however, more and more localized transient reconnections, dipolarization fronts, and bursty bulk flows heat the ions and cumulatively increase the ion temperature (see Figure 7). Thus, we suggest that the discrepancy between observed and simulated magnetotail ion temperatures would be diminished in sufficiently long time simulations.

4. Probing the Distant Tail From the Near-Earth Observations

Using the simulation results presented in section 3, we plot, in Figure 8, the ion temperature profile $T_i(B_x)$ at $x = -15\ R_E$ with different colors indicating the location of the equatorial origin of the corresponding ion population. According to this figure, the ions that contribute to the ion temperature measured at $B_x \approx \pm 15$ nT come along magnetic field lines from the equatorial source at $x \approx -15\ R_E$. Making similar mappings, we find that the ions measured at $B_x \approx \pm 30$ nT and $B_x \approx \pm 40$ nT originated from $x \approx -35\ R_E$ and $x \approx -55\ R_E$, respectively. These mappings coincide with the statistical results collected by THEMIS (see Figure 3, the colored circles at the black temperature profile and their corresponding colored temperature profiles). For example, the red circle indicates that the ion temperature at $r \in [9, 12]\ R_E$ when $B_x \approx 27$ nT is mapped from the tailward region $r \in [22, 30]\ R_E$ in the neutral sheet ($B_x \approx 0$). We should mention that the absolute values of ion temperature obtained in simulations (Figure 8) are lower than the observed values (Figure 3), the discrepancy will be explained in section 6. We focus on comparison of relative values, i.e., we consider downtail locations of the equatorial sources of ions contributing to the $T_i(B_x)$ profile measured at the near-Earth region.

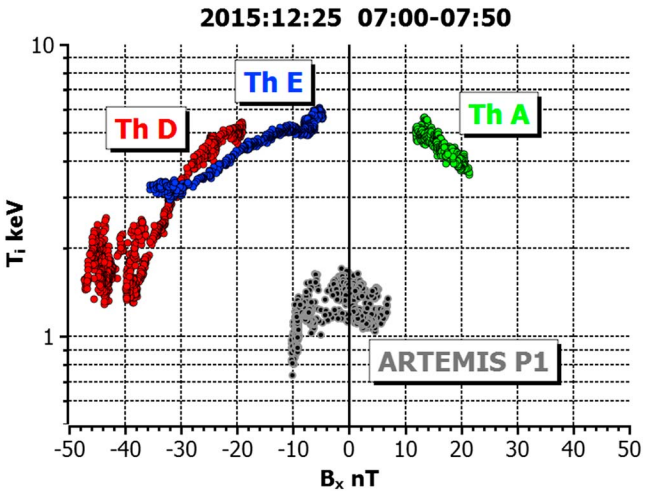

Figure 9. Ion temperature T_i measured simultaneously by three THEMIS spacecraft at $x = -10\ R_E$ and ARTEMIS P1 at $x = -58\ R_E$. All spacecraft are located at midnight ($|y| < 2\ R_E$).

To use spacecraft observations to verify the above hybrid simulation results, we need to compare the ion temperature measured simultaneously at the entire current sheet, in the near-Earth region, and the distant tail. For this reason, we use a current sheet thinning event measured by three THEMIS spacecraft in the near-Earth tail, during which intense current, peaked at the equator, is observed [see *Artemyev et al.*, 2016a]. The current intensifies with time, increasing the magnetic field gradient and causing the spacecraft to move closer to the current sheet boundary. Observations of ion temperature by THEMIS A, THEMIS

D, and THEMIS E during this event are shown in Figure 9. All three spacecraft are located at around midnight ($y \approx 0$) and slightly separated along the x and z directions. The measurements at different sides of the equatorial plane allow us to confirm the general bell-shaped profile of the ion temperature. THEMIS D reached the current sheet boundary at $B_x \approx -40$ nT, where the measured ion temperature $T_i \approx 1.5$ keV. Figure 8 suggests that these ions come from the downtail distance at $x \approx -55\ R_E$. At the same time, ARTEMIS P1, near the Moon, was probing the distant ($x \approx -58\ R_E$) current sheet, also around midnight ($y \approx 0$). Its temperature profile (see Figure 9) shows that ARTEMIS at the equator, at $x \approx -58\ R_E$, measured the same ion temperature, $T_i \approx 1.5$ keV, as THEMIS D observed at the current sheet boundary ($B_x \approx -40$ nT) at $x \approx -10\ R_E$. Therefore, the simulation results shown in Figure 8 correctly predict the distant tail equatorial source of ions observed in the near-Earth current sheet boundary.

Comparison of Figures 8 and 9 demonstrates that the hybrid simulations can well describe the magnetotail configuration within the entire domain, $x \in [-60, -10]\ R_E$. We correctly reproduce the 2-D (x-z) geometry of magnetic field lines connecting the near-Earth current sheet to the equatorial magnetotail as far away as lunar orbit. Thus, using both hybrid simulations and near-Earth magnetotail measurements, we ascertain our expectation that the earthward temperature gradient maps magnetically into (and is thus consistent with) the vertical temperature gradient. Using this information, it is now possible to construct the plasma conditions and a realistic magnetic field configuration in the entire magnetotail during quiet times.

5. Theoretical Approaches for $T_i(B_x)$ Modeling

The multispacecraft observations and hybrid simulations presented in sections 2–4 demonstrate that the $T_i(B_x)$ bell-shaped profiles represent the typical ion temperature distribution in the magnetotail. This distribution can influence local current sheet properties, such as current sheet stability. Investigation of such properties requires self-consistent kinetic simulations (using particle-in-cell codes [e.g., *Goldman et al.*, 2016, and reference therein] or Vlasov codes [e.g., *Büchner and Elkina*, 2005; *Hoilijoki et al.*, 2017]] with the initial conditions describing current sheets, including $T_i(B_x)$ profiles. However, the majority of present kinetic models are generalizations of the Harris model [*Harris*, 1962] with $T_i = \text{const}$. Therefore, in this section, we include the observed bell-shaped temperature profile in kinetic current sheet models. For this reason, we consider possible generalizations of simple equilibrium solutions of the Vlasov-Maxwell system of equations for current sheets. We use the approach proposed by *Schindler* [1972] and *Lembège and Pellat* [1982], which assumes that the current sheet is a stationary 2-D (in the x-z plane) plasma equilibrium supported by diamagnetic currents of ions and electrons. Stationarity and homogeneity of the system along the y (dawn-dusk) direction provide two integrals of motion: generalized momentum $p_{y\alpha}$ and total particle energy H_α:

$$\begin{aligned} p_{y\alpha} &= m_\alpha v_y + \frac{q_\alpha}{c} A_y \\ H_\alpha &= \frac{1}{2} m_\alpha \left(v_x^2 + v_z^2\right) + \frac{1}{2m_\alpha}\left(p_{y\alpha} - \frac{q_\alpha}{c} A_y\right) + q_\alpha \varphi \end{aligned}, \tag{1}$$

where α=i, e for ions and electrons; $q_\alpha = \pm e$ is the charge of particles; m_α is the mass of particles; v_x, v_y, v_z are velocity components; and $A_y = A_y(x, z)$ and $\varphi = \varphi(x, z)$ are the vector and scalar potential components, respectively. Any distribution function $f_\alpha = f_\alpha(H_\alpha, p_{y\alpha})$ then is a solution of Vlasov equation. The standard approach for constructing equilibrium solutions is choosing such an f_α that the corresponding solutions of Maxwell's equations (i.e., electric and magnetic fields) satisfy the required spatial distribution (see, e.g., examples in *Schindler and Birn* [2002], *Birn et al.* [2004], and *Yoon and Lui* [2004]). We choose a rather general form of f_α:

$$f_\alpha = n_0 \left(\frac{m_\alpha}{2\theta_\alpha \pi}\right)^{3/2} \exp(-H_\alpha/\theta_\alpha)\, g\left(v_{D\alpha} p_{y\alpha}/\theta_\alpha\right), \tag{2}$$

where n_0 is a typical plasma density, θ_α is a parameter defining the thermal spread of the velocity distribution (effective temperature), $v_{D\alpha}$ is a parameter to determine the particle current density magnitude, and $g()$ is some finite function. For $g = \exp(v_{D\alpha} p_{y\alpha}/\theta_\alpha)$, we obtain the classical Harris solution [*Harris*, 1962] and all its 2-D generalizations [e.g., *Schindler*, 1972; *Lembège and Pellat*, 1982; *Tur et al.*, 2001; *Sitnov and Schindler*, 2010].

Zero- and second-order moments (density and pressure) of the distribution (2) can be written as

$$\begin{aligned} n_\alpha &= n_0 e^{-q_\alpha\varphi/T_\alpha} R(\eta_\alpha, \eta_\alpha a_\alpha) \\ P_\alpha &= \theta_\alpha n_0 e^{-q_\alpha\varphi/T_\alpha} R(\eta_\alpha, \eta_\alpha a_\alpha) \end{aligned}, \tag{3}$$

where

$$R = \pi^{-1/2} \iint_{-\infty}^{+\infty} g(\eta_\alpha u + a_\alpha) e^{-u^2}\, du, a_\alpha = \eta_\alpha \frac{q_\alpha A_y}{c\sqrt{2\theta_\alpha m_\alpha}}, \eta_\alpha = v_{D\alpha}\sqrt{\frac{m_\alpha}{2\theta_\alpha}}. \tag{4}$$

We use the following normalization of the vector potential and g function: $A_y = 0$ for $z = 0$ at the chosen x coordinate and $R = 1$ for $a_\alpha = 0$. The magnetic field $B_x = -\partial A_y/\partial z$ goes to a constant at $z \to \pm\infty$; thus, $A_y \sim z$ at $z \to \pm\infty$. As g is a finite function, we have $g \to 0$ for $a_\alpha \sim A_y \to \pm\infty$. Therefore, $R = 1$ at the neutral plane ($z = 0$), and $R \to 0$ at the current sheet boundaries ($z \to \pm\infty$). These two important properties allow us to analyze the profiles of particle temperature $T_\alpha = P_\alpha/n_\alpha$ without specifying g. The simplest model, equation (3), has a uniform temperature $T_\alpha = P_\alpha/n_\alpha = \theta_\alpha$. In the following, we will consider two generalizations of model (2). We will assume $f_\alpha = f_\alpha(\theta_\alpha, \eta_\alpha)$, i.e., f_α depends only on θ_α and η_α.

5.1. Effect of Background Plasma

Let us consider that the distribution function consists of current carrying particles and background plasma:

$$F_\alpha = (1-\delta) f_\alpha(\theta_\alpha, \eta_\alpha) + \delta f_\alpha\left(\theta_{\alpha,bg}, 0\right), \tag{5}$$

where f_α is given by equation (2), $\delta \in [0, 1]$ defines relative density of the background, and $\theta_{\alpha,bg}$ is the background effective temperature. The second (background) distribution in equation (5) does not provide any current, because $\eta_\alpha = 0$. The two moments of distribution (5) can be written as

$$\begin{aligned} n_\alpha &= (1-\delta) n_0 e^{-q_\alpha\varphi/\theta_\alpha} R(\eta_\alpha) + \delta n_0 e^{-q_\alpha\varphi/\theta_{\alpha,bg}} \\ P_\alpha &= (1-\delta) n_0 \theta_\alpha e^{-q_\alpha\varphi/\theta_\alpha} R(\eta_\alpha) + \delta n_0 \theta_{\alpha,bg} e^{-q_\alpha\varphi/\theta_{\alpha,bg}} \end{aligned}. \tag{6}$$

The quasi-neutrality condition $\sum_\alpha q_\alpha n_\alpha = 0$ has a solution, $\varphi = 0$. Using this solution, we obtain the expression for temperature:

$$T_\alpha = \frac{P_\alpha}{n_\alpha} = \frac{(1-\delta)\theta_\alpha R(\eta_\alpha) + \delta\theta_{\alpha,bg}}{(1-\delta) R(\eta_\alpha) + \delta}. \tag{7}$$

At the neutral plane, where $R = 1$, we have $T_{\alpha 0} = (1-\delta)\theta_\alpha + \delta\theta_{\alpha,bg}$, and at the current sheet boundaries, where $R \to 0$, we have $T_{\alpha\infty} = \theta_{\alpha,bg}$ (this expression works for any $\delta \neq 0$, whereas for $\delta = 0$ we have $T_\alpha = \theta_\alpha$). Figure 10 shows the ratio $T_{\alpha 0}/T_{\alpha\infty} = (1-\delta)(\theta_\alpha/\theta_{\alpha,bg}) + \delta$ as function of $n_{\alpha 0}/n_{\alpha\infty} = \delta$ and $\theta_\alpha/\theta_{\alpha,bg}$. In the system with small background plasma density ($\delta \sim 0.1$–0.25), the temperature can decrease significantly at the current sheet boundary if the background is sufficiently cold ($\theta_\alpha/\theta_{\alpha,bg} > 5$). This effect provides a bell-shaped temperature distribution; thus, kinetic model (5) can mimic the observed properties of the current sheet.

To plot the T_α profile defined by equation (7), one needs to determine the particle velocity distribution (2) and the corresponding R function. For a Harris-type $g = \exp(v_{D\alpha} p_{y\alpha}/\theta_\alpha)$ function, we obtain $R \sim \exp(a_\alpha) \sim \cosh^2(z/L) \sim 1 - (B_x/B_0)^2$ with the magnetic field $B_x = B_0 \tanh(z/L)$ [*Harris*, 1962]. Figure 10 shows several examples of $T_\alpha(B_x)$ profiles for different system parameters. The general shape of $T_\alpha(B_x)$ resembles that obtained from observations and hybrid simulations. However, independent to the background plasma fraction, δ, the boundary temperature for all profiles equals to $\theta_{\alpha,bg}$.

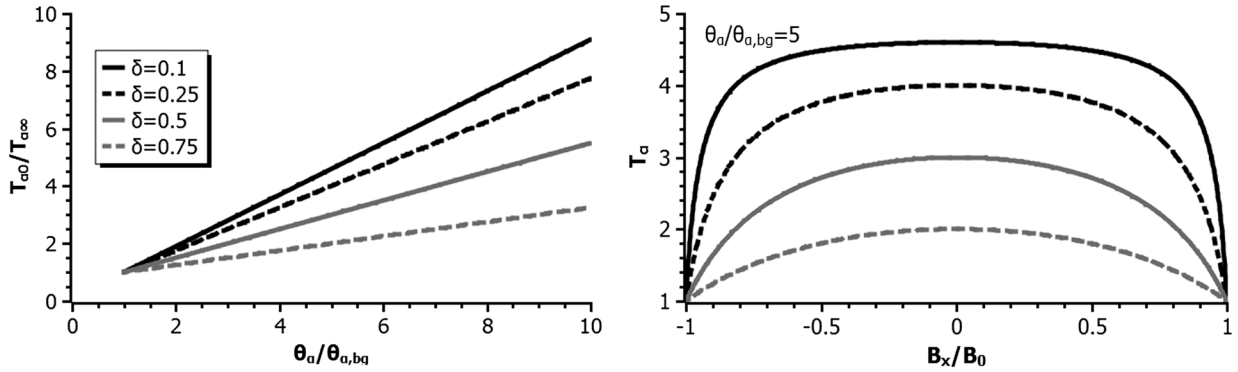

Figure 10. (left) $T_{\alpha 0}/T_{\alpha\infty}$ as function of $n_{\alpha 0}/n_{\alpha\infty}=\delta$ and $\theta_\alpha/\theta_{\alpha,bg}$ for kinetic current sheet model (5). (right) Profiles $T_\alpha(B_x)/\theta_{\alpha,bg}$ given by equation (7) for $\theta_\alpha/\theta_{\alpha,bg}=5$ and different δ.

5.2. Synthetic Distribution

In this subsection we consider the synthetic distribution function proposed by *Catapano et al.* [2015]:

$$F_\alpha = f_\alpha(\theta_{\alpha 1},\eta_\alpha) - f_\alpha(\theta_{\alpha 2},\eta_\alpha) + \delta f_\alpha\left(\theta_{\alpha,bg},0\right), \tag{8}$$

where the last term corresponds to the background plasma. Zero- and second-order moments of (8) can be written as

$$\begin{aligned} n_\alpha &= n_0 e^{-q_\alpha\varphi/\theta_{\alpha 1}}R(\eta_\alpha) - n_0 e^{-q_\alpha\varphi/\theta_{\alpha 2}}R(\eta_\alpha) + \delta n_0 \\ P_\alpha &= n_0 R(\eta_\alpha)\left(\theta_{\alpha 1}e^{-q_\alpha\varphi/\theta_{\alpha 1}} - \theta_{\alpha 2}e^{-q_\alpha\varphi/\theta_{\alpha 2}}\right) + \delta n_0\theta_{\alpha,bg}e^{-q_\alpha\varphi/\theta_{\alpha,bg}} \end{aligned}. \tag{9}$$

Here, too, the quasi-neutrality condition $\sum_\alpha q_\alpha n_\alpha = 0$ has a solution $\varphi = 0$. Using this solution, we rewrite equation (9):

$$n_\alpha = \delta n_0, \quad P_\alpha = n_0 R(\eta_\alpha)(\theta_{\alpha 1} - \theta_{\alpha 2}) + \delta n_0\theta_{\alpha,bg}. \tag{10}$$

Equation (10) shows that the proposed solution has a uniform plasma density, whereas the plasma pressure P_α has the same profile as in equation (6). The main difference between equations (10) and (6) is that the plasma pressure across the current sheet for distribution (8) comes entirely from plasma temperature variation

$$T_\alpha = \frac{P_\alpha}{n_\alpha} = R(\eta_\alpha)(\theta_{\alpha 1} - \theta_{\alpha 2})/\delta + \theta_{\alpha,bg}. \tag{11}$$

Two conditions must be satisfied for distribution (8): $\theta_{\alpha 1} > \theta_{\alpha 2}$ and the background density should be large enough to exclude the possible negative values of the phase space density. The ratio $T_{\alpha 0}/T_{\alpha\infty}$ for equation (11) takes the form

$$\frac{T_{\alpha 0}}{T_{\alpha\infty}} = 1 + \frac{\theta_{\alpha 1} - \theta_{\alpha 2}}{\delta\theta_{\alpha,bg}}. \tag{12}$$

Figure 11 shows how the temperature ratio (12) depends on the background plasma density and temperature. For a cold background, ratio (12) is large enough, i.e., temperature decreases significantly toward the current sheet boundary. Comparison of Figures 10 and 11 shows that these two models provide different ranges of δ: for model (8) we can use a more realistic dense background plasma, whereas model (5) requires a rarified background. One can consider a more general version of model (8) in which the densities of the two

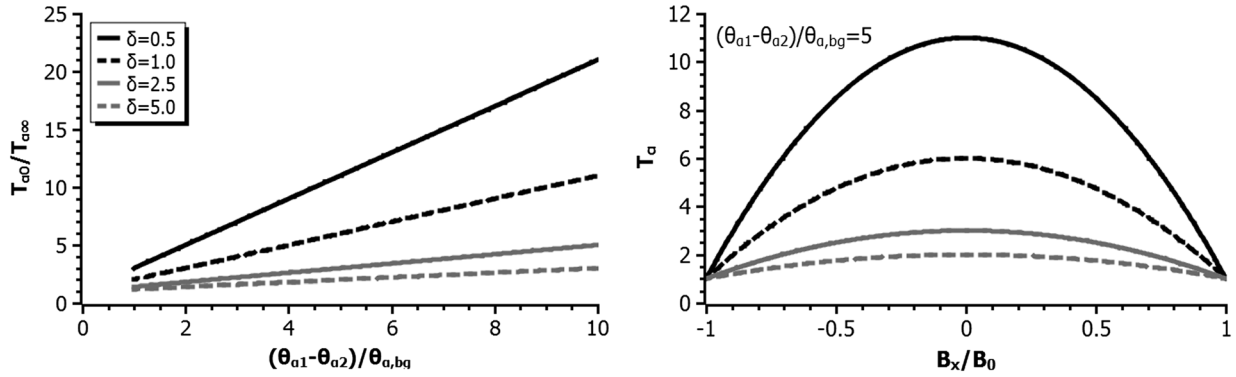

Figure 11. (left) Ratio $T_{\alpha 0}/T_{\alpha\infty}$ as function of $n_{\alpha 0}/n_{\alpha\infty}=\delta$ and $(\theta_{\alpha 1}-\theta_{\alpha 2})/\theta_{\alpha,bg}$ for kinetic current sheet model (8). (right) Profiles $T_\alpha(B_x)/\theta_{\alpha,bg}$ given by equation (11) for $(\theta_{\alpha 1}-\theta_{\alpha 2})/\theta_{\alpha,bg}=5$ and different δ.

first populations are different. In this case, both temperature and density vary across the current sheet [see *Catapano et al.*, 2015].

To plot the profile of T_α as defined by equation (11), one can use a Harris-type $g=\exp(v_{D\alpha}p_{y\alpha}/\theta_\alpha)$ function for the particle velocity distribution in equation (2). The corresponding spatial distribution of the plasma is given by function $\sim\exp(a_\alpha)\sim\cosh^2(z/L)\sim 1-(B_x/B_0)^2$, with the magnetic field $B_x=B_0\tanh(z/L)$ [*Harris*, 1962]. Figure 11 shows several $T_\alpha(B_x)$ profiles for different $(\theta_{\alpha 1}-\theta_{\alpha 2})/\delta$ values. In contrast to Figure 10 ($T_\alpha(B_x)$ profiles for Harris model with the background plasma, the shape of $T_\alpha(B_x)$ for model (8) does not depend on the system parameters, i.e., only the magnitude of the particle temperature can be changed.

The phase space density distributions of the two models (5) and (8) are also different. Figure 12 shows two distributions in the (v_x, v_y) velocity plane. Distribution (5) has a distinct hot (current-carrying) population superimposed on the cold background population. Similar distributions are observed in thin current sheets before/after reconnection onset [e.g., *Zhou et al.*, 2009, 2016]. Distribution (8) has an almost symmetrical hot population with slightly increased phase space density at $v_y>0$. Such a distribution is often observed in a relatively thin current sheet [e.g., *Artemyev et al.*, 2009, 2010]. The distributions are plotted in the v_x-v_y plane, perpendicular to the magnetic field B_z direction (because these distributions are plotted in the neutral plane where $B_x=0$ and only $B_z\neq 0$). Therefore, the asymmetry of the ion distributions in the plane corresponds to the nongyrotropy in the perpendicular plane. The distributions are symmetric relative to v_z (parallel direction) and thus do not provide any field-aligned flow. The obtained nongyrotropy is due to the particle diamagnetic drifts in y direction, i.e., the distributions are asymmetric along v_y but symmetric along v_x and v_z.

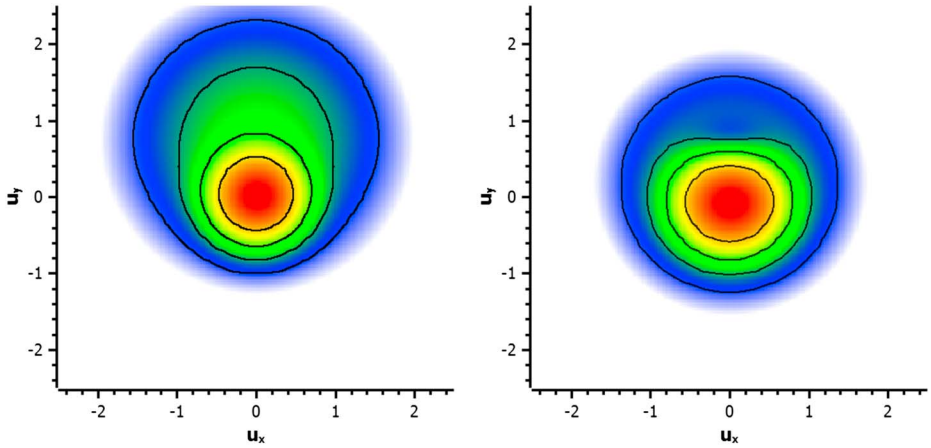

Figure 12. Distribution functions $(v_z=0, u_{x,y}=v_{x,y}(m_\alpha/2\theta_\alpha)^{1/2})$ for models (left) (5) and (right) (8) in the neutral plane ($B_x=0$), i.e., the distributions are shown in the plane transverse to the magnetic field direction. System parameters are for model (5) $\delta=0.25$, $\theta_{\alpha,bg}/\theta_\alpha=0.25$ and for model (8) $\delta=2.5$, $\theta_{\alpha,bg}/\theta_{\alpha 1}=0.25$, $\theta_{\alpha 2}/\theta_{\alpha 1}=0.25$.

Further comparisons of temperature profiles and velocity distributions in the two kinetic models (see Figures 10–12) with those obtained from hybrid simulations and spacecraft observations (during quiet times before reconnection and its resultant structures perturb the magnetotail current sheet) are needed and will be left to future studies.

6. Summary and Discussion

Using (1) simultaneous THEMIS D, Geotail, and ARTEMIS P1 observations between $x \approx -10\ R_E$ and lunar orbit and (2) statistics collected by THEMIS four spacecraft in the near-Earth magnetotail, we showed that the $T_i(B_x)$ profiles are ubiquitously bell shaped in the magnetotail. We used 3-D global hybrid simulations to describe how these profiles are formed. According to the simulation results, in the absence of a field-aligned gradient of the ion temperature, the $T_i(x)$ profile is mapped along magnetic field lines and forms the bell-shaped $T_i(B_x)$ profile in the z direction. By ascertaining the mapping of the ion temperature along magnetic field lines in the magnetotail, it is possible to use this knowledge to reconstruct two-dimensional maps of these quantities from vertical spacecraft crossings. The combination of spacecraft observations and global hybrid simulations demonstrates that the bell-shaped $T_i(B_x)$ profile is an intrinsic property of Earth's magnetotail that should be taken into account in kinetic descriptions of the magnetotail. Using theoretical approaches, we have included the temperature gradient in kinetic current sheet models.

The global simulation results shown in Figures 4–8 were obtained for stable but rather fast solar wind, 700 km/s. Under these conditions, the magnetotail with a thermal ion population forms faster. We performed an additional simulation run with slow solar wind, 350 km/s. In that case too, although the magnetotail ions need more time to establish a quasi-stationary temperature distribution within the tail, bell-shaped $T_i(B_x)$ profiles are eventually formed. On the other hand, in the observation shown in Figure 9, the corresponding solar wind speed varies from 500 km/s to 530 km/s. Although the solar wind speed is different in the observation and simulations (700 km/s and 350 km/s), they all show the bell-shaped $T_i(B_x)$ profile and the distant tail probing using the near-Earth current sheet crossings. This shows that although the magnetotail ion temperature quantitatively depends on the solar wind characteristics, the essential properties and mechanism of ion temperature distribution are not changed by the solar wind.

Acknowledgments

We acknowledge NASA contract NAS5-02099. We would like to thank the following people, specifically C.W. Carlson and J.P. McFadden for the use of ESA data; D.E. Larson for the use of SST data; and K.H. Glassmeier, U. Auster, and W. Baumjohann for the use of FGM data provided under the lead of the Technical University of Braunschweig and with financial support through the German Ministry for Economy and Technology and the German Aerospace Center (DLR) under contract 50 OC 0302. We thank J. Hohl for her assistance in the manuscript editing. The computer resources were provided by the Extreme Science and Engineering Discovery Environment (XSEDE). All spacecraft data were downloaded from http://themis.ssl.berkeley.edu/ and http://cdaweb.gsfc.nasa.gov/. All simulation data can be obtained by contacting the corresponding author through e-mail. Processed spacecraft data and simulation results supporting the figures reported in this work can be accessed by writing to the following addresses: slu@igpp.ucla.edu and aartemyev@igpp.ucla.edu.

References

Angelopoulos, V. (2008), The THEMIS mission, *Space Sci. Rev.*, *141*, 5–34, doi:10.1007/s11214-008-9336-1.

Artemyev, A. V., A. A. Petrukovich, L. M. Zelenyi, R. Nakamura, H. V. Malova, and V. Y. Popov (2009), Thin embedded current sheets: Cluster observations of ion kinetic structure and analytical models, *Ann. Geophys.*, *27*, 4075–4087.

Artemyev, A. V., A. A. Petrukovich, R. Nakamura, and L. M. Zelenyi (2010), Proton velocity distribution in thin current sheets: Cluster observations and theory of transient trajectories, *J. Geophys. Res.*, *115*, A12255, doi:10.1029/2010JA015702.

Artemyev, A. V., A. A. Petrukovich, R. Nakamura, and L. M. Zelenyi (2011), Cluster statistics of thin current sheets in the Earth magnetotail: Specifics of the dawn flank, proton temperature profiles and electrostatic effects, *J. Geophys. Res.*, *116*, A0923, doi:10.1029/2011JA016801.

Artemyev, A. V., V. N. Lutsenko, and A. A. Petrokovich (2012), Ion resonance acceleration by dipolarization fronts: Analytic theory and spacecraft observation, *Ann. Geophys.*, *30*, 317–324, doi:10.5194/angeo-30-317-2012.

Artemyev, A. V., V. Angelopoulos, A. Runov, and A. A. Petrokovich (2016a), Properties of current sheet thinning at $x \sim -10$ to $-12\ R_E$, *J. Geophys. Res. Space Physics*, *121*, 6718–6731, doi:10.1002/2016JA022779.

Artemyev, A. V., V. Angelopoulos, and A. Runov (2016b), On the radial force balance in the quiet time magnetotail current sheet, *J. Geophys. Res. Space Physics*, *121*, 4017–4026, doi:10.1002/2016JA022480.

Artemyev, A. V., V. Angelopoulos, H. Hietala, A. Runov, and I. Shinohara (2017), Ion density and temperature profiles along (X_{GSM}) and across (Z_{GSM}) the magnetotail as observed by THEMIS, Geotail, and ARTEMIS, *J. Geophys. Res. Space Physics*, *122*, 1590–1599, doi:10.1002/2016JA023710.

Ashour-Abdalla, M., L. M. Zelenyi, V. Peroomian, and R. L. Richard (1994), Consequences of magnetotail ion dynamics, *J. Geophys. Res.*, *99*, 14,891–14,916, doi:10.1029/94JA00141.

Auster, H. U., et al. (2008), The THEMIS fluxgate magnetometer, *Space Sci. Rev.*, *141*, 235–264, doi:10.1007/s11214-008-9365-9.

Birn, J., K. Schindler, and M. Hesse (2004), Thin electron current sheets and their relation to auroral potentials, *J. Geophys. Res.*, *109*, A02217, doi:10.1029/2003JA010303.

Birn, J., M. Hesse, R. Nakamura, and S. Zaharia (2013), Particle acceleration in dipolarization events, *J. Geophys. Res. Space Physics*, *118*, 1960–1971, doi:10.1002/jgra.50132.

Büchner, J., and N. Elkina (2005), Vlasov code simulation of anomalous resistivity, *Space Sci. Rev.*, *121*(1–4), 237–252.

Catapano, F., A. V. Artemyev, G. Zimbardo, and I. Y. Vasko (2015), Current sheets with inhomogeneous plasma temperature: Effects of polarization electric field and 2D solutions, *Phys. Plasmas*, *22*(9), 092905, doi:10.1063/1.4931736.

Drake, J. F., M. Swisdak, T. D. Phan, P. A. Cassak, M. A. Shay, S. T. Lepri, R. P. Lin, E. Quataert, and T. H. Zurbuchen (2009), Ion heating resulting from pickup in magnetic reconnection exhausts, *J. Geophys. Res.*, *114*, A05111, doi:10.1029/2008JA013701.

Dungey, J. W. (1963), Interactions of solar plasma with the geomagnetic field, *Planet. Space Sci.*, *10*, 233–237, doi:10.1016/0032-0633(63)90020-5.

Goldman, M. V., D. L. Newman, and G. Lapenta (2016), What can we learn about magnetotail reconnection from 2D PIC Harris-sheet simulations?, *Space Sci. Rev.*, *199*(1–4), 651–688.
Guild, T. B., H. E. Spence, E. L. Kepko, V. Merkin, J. G. Lyon, M. Wiltberger, and C. C. Goodrich (2008), Geotail and LFM comparisons of plasma sheet climatology: 1. Average values, *J. Geophys. Res.*, *113*, A04216, doi:10.1029/2007JA012611.
Harris, E. (1962), On a plasma sheet separating regions of oppositely directed magnetic field, *Nuovo Cimento*, *23*, 115–121.
Hietala, H., J. F. Drake, T. D. Phan, J. P. Eastwood, and J. P. McFadden (2015), Ion temperature anisotropy across a magnetotail reconnection jet, *Geophys. Res. Lett.*, *42*, 7239–7247, doi:10.1002/2015GL065168.
Hoilijoki, S., U. Ganse, Y. Pfau-Kempf, P. A. Cassak, B. M. Walsh, H. Hietala, S. von Alfthan, and M. Palmroth (2017), Reconnection rates and X-line motion at the magnetopause: Global 2D-3V hybrid-Vlasov simulation results, *J. Geophys. Res. Space Physics*, *122*, 2877–2888, doi:10.1002/2016JA02370.
Hoshino, M., A. Nishida, T. Mukai, Y. Saito, T. Yamamoto, and S. Kokubun (1996), Structure of plasma sheet in magnetotail: Double-peaked electric current sheet, *J. Geophys. Res.*, *101*, 24,775–24,786, doi:10.1029/96JA02313.
Karimabadi, H., et al. (2014), The link between shocks, turbulence, and magnetic reconnection in collisionless plasmas, *Phys. Plasmas*, *21*, 062308, doi:10.1063/1.4882875.
Kaufmann L. R., C. Lu, W. R. Paterson and L. A. Frank (2002), Three-dimensional analyses of electric currents and pressure anisotropies in the plasma sheet, *J. Geophys. Res.*, *107*(A7), 1103, doi:10.1029/2001JA000288.
Kissinger, J., R. L. McPherron, T.-S. Hsu, and V. Angelopoulos (2012), Diversion of plasma due to high pressure in the inner magnetosphere during steady magnetospheric convection, *J. Geophys. Res.*, *117*, A05206, doi:10.1029/2012JA017579.
Kokubun, S., T. Yamamoto, M. H. Acuna, K. Hayashi, K. Shiokawa, and H. Kawano (1994), The GEOTAIL magnetic field experiment, *J. Geomagn. Geoelectr.*, *46*, 7–21.
Lembège, B., and R. Pellat (1982), Stability of a thick two-dimensional quasineutral sheet, *Phys. Fluids*, *25*, 1995–2004, doi:10.1063/1.863677.
Lin, Y., X. Y. Wang, S. Lu, J. D. Perez, and Q. M. Lu (2014), Investigation of storm-time magnetotail and ion injection using three-dimensional global hybrid simulation, *J. Geophys. Res. Space Physics*, *119*, 7413–7432, doi:10.1002/2014JA020005.
Lin, Y., S. Wing, J. R. Johnson, X. Y. Wang, J. D. Perez, and L. Cheng (2017), Formation and transport of entropy structures in the magnetotail simulated in a 3-D global hybrid code, *Geophys. Res. Lett.*, *44*, 5892–5899, doi:10.1002/2017GL073957.
Lu, S., Y. Lin, Q. M. Lu, X. Y. Wang, R. S. Wang, C. Huang, M. Y. Wu, and S. Wang (2015a), Evolution of flux ropes in the magnetotail: A three-dimensional global hybrid simulation, *Phys. Plasmas*, *22*(5), 052901, doi:10.1063/1.4919615.
Lu, S., et al. (2015b), Dipolarization fronts as earthward propagating flux ropes: A three-dimensional global hybrid simulation, *J. Geophys. Res. Space Physics*, *120*, 6286–6300, doi:10.1002/2015JA021213.
Lu, S., V. Angelopoulos, and H. Fu (2016a), Suprathermal particle energization in dipolarization fronts: Particle-in-cell simulations, *J. Geophys. Res. Space Physics*, *121*, 9483–9500, doi:10.1002/2016JA022815.
Lu, S., Y. Lin, V. Angelopoulos, A. V. Artemyev, P. L. Pritchett, Q. Lu, and X. Y. Wang (2016b), Hall effect control of magnetotail dawn-dusk asymmetry: A three-dimensional global hybrid simulation, *J. Geophys. Res. Space Physics*, *121*, 11,882–11,895, doi:10.1002/2016JA023325.
Lyons, L. R. (1984), Electron energization in the geomagnetic tail current sheet, *J. Geophys. Res.*, *89*, 5479–5487, doi:10.1029/JA089iA07p05479.
McFadden, J. P., C. W. Carlson, D. Larson, M. Ludlam, R. Abiad, B. Elliott, P. Turin, M. Marckwordt, and V. Angelopoulos (2008), The THEMIS ESA plasma instrument and inflight calibration, *Space Sci. Rev.*, *141*, 277–302, doi:10.1007/s11214-008-9440-2.
Mukai, T., S. Machida, Y. Saito, et al. (1994), The low energy particles (LEP) experiment onboard the GEOTAIL satellite, *J. Geomagn. Geoelectr.*, *46*, 669–692.
Raeder, J., R. J. Walker, and M. Ashour-Abdalla (1995), The structure of the distant geomagnetic tail during long periods of northward IMF, *Geophys. Res. Lett.*, *22*, 349–352, doi:10.1029/94GL03380.
Runov, A., et al. (2006), Local structure of the magnetotail current sheet: 2001 Cluster observations, *Ann. Geophys.*, *24*, 247–262.
Schindler, K. (1972), A self-consistent theory of the tail of the magnetosphere, in *Earth's Magnetospheric Processes, Astrophysics and Space Science Library*, vol. 32, edited by B. M. McCormac, pp. 200–209, D. Reidal, Dordrecht, Netherlands.
Schindler, K. (2006), *Physics of Space Plasma Activity*, Cambridge Univ. Press, Cambridge, U. K.
Schindler, K., and J. Birn (2002), Models of two-dimensional embedded thin current sheets from Vlasov theory, *J. Geophys. Res.*, *107*(A8), 1193, doi:10.1029/2001JA000304.
Sergeev, V. A., D. A. Sormakov, S. V. Apatenkov, W. Baumjohann, R. Nakamura, A. V. Runov, T. Mukai, and T. Nagai (2006), Survey of large-amplitude flapping motions in the midtail current sheet, *Ann. Geophys.*, *24*, 2015–2024.
Sitnov, M. I., and V. G. Merkin (2016), Generalized magnetotail equilibria: Effects of the dipole field, thin current sheets, and magnetic flux accumulation, *J. Geophys. Res. Space Physics*, *121*, 7664–7683, doi:10.1002/2016JA023001.
Sitnov, M. I., and K. Schindler (2010), Tearing stability of a multiscale magnetotail current sheet, *Geophys. Res. Lett.*, *37*, L08102, doi:10.1029/2010GL042961.
Sitnov, M. I., L. M. Zelenyi, H. V. Malova, and A. S. Sharma (2000), Thin current sheet embedded within a thicker plasma sheet: Self-consistent kinetic theory, *J. Geophys. Res.*, *105*, 13,029–13,044, doi:10.1029/1999JA000431.
Sitnov, M. I., M. Swisdak, P. N. Guzdar, and A. Runov (2006), Structure and dynamics of a new class of thin current sheets, *J. Geophys. Res.*, *111*, A08204, doi:10.1029/2005JA011517.
Slavin, J. A., E. J. Smith, D. G. Sibeck, D. N. Baker, and R. D. Zwickl (1985), An ISEE 3 study of average and substorm conditions in the distant magnetotail, *J. Geophys. Res.*, *90*, 10,875–10,895, doi:10.1029/JA090iA11p10875.
Speiser, T. W. (1965), Particle trajectories in model current sheets: 1. Analytical solutions, *J. Geophys. Res.*, *70*, 4219–4226, doi:10.1029/JZ070i017p04219.
Stiles, G. S., E. W. Hones Jr., S. J. Bame, and J. R. Asbridge (1978), Plasma sheet pressure anisotropies, *J. Geophys. Res.*, *83*, 3166–3172, doi:10.1029/JA083iA07p03166.
Tur, A., P. Louarn, V. Yanovsky, D. Le Queau, and V. Genot (2001), On the asymptotic theory of localized structures in a thin two-dimensional Harris current sheet: Plasmoids, multiplasmoids and X points, *J. Plasma Phys.*, *66*, 97–117, doi:10.1017/S002237780100112X.
Wang, C.-P., L. R. Lyons, T. Nagai, and J. C. Samson (2004), Midnight radial profiles of the quiet and growth-phase plasma sheet: The Geotail observations, *J. Geophys. Res.*, *109*, A12201, doi:10.1029/2004JA010590.
Wang, C.-P., L. R. Lyons, J. M. Weygand, T. Nagai, and R. W. McEntire (2006), Equatorial distributions of the plasma sheet ions, their electric and magnetic drifts, and magnetic fields under different interplanetary magnetic field B_z conditions, *J. Geophys. Res.*, *111*, A04215, doi:10.1029/2005JA011545.
Wang, C.-P., S. G. Zaharia, L. R. Lyons, and V. Angelopoulos (2013), Spatial distributions of ion pitch angle anisotropy in the near-Earth magnetosphere and tail plasma sheet, *J. Geophys. Res. Space Physics*, *118*, 244–255, doi:10.1029/2012JA018275.

Wing, S., and P. T. Newell (1998), Central plasma sheet ion properties as inferred from ionospheric observations, *J. Geophys. Res.*, *103*, 6785–6800, doi:10.1029/97JA02994.

Wing, S., and P. T. Newell (2002), 2D plasma sheet ion density and temperature profiles for northward and southward IMF, *Geophys. Res. Lett.*, *29*(9), 1307, doi:10.1029/2001GL013950.

Wing, S., et al. (2014), Review of solar wind entry into the transport within the plasma sheet, *Space Sci. Rev.*, *184*(1–4), 33–86, doi:10.1007/s11214-014-0108-9.

Yoon, P. H., and A. T. Y. Lui (2004), Model of ion- or electron-dominated current sheet, *J. Geophys. Res.*, *109*, A11213, doi:10.1029/2004JA010555.

Yoon, P. H., and A. T. Y. Lui (2005), A class of exact two-dimensional kinetic current sheet equilibria, *J. Geophys. Res.*, *110*, A01202, doi:10.1029/2003JA010308.

Zelenyi, L. M., M. I. Sitnov, H. V. Malova, and A. S. Sharma (2000), Thin and superthin ion current sheets. Quasi-adiabatic and nonadiabatic models, *Nonlinear Process. Geophys.*, *7*, 127–139.

Zelenyi, L. M., H. V. Malova, A. V. Artemyev, V. Y. Popov, and A. A. Petrukovich (2011), Thin current sheets in collisionless plasma: Equilibrium structure, plasma instabilities, and particle acceleration, *Plasma Phys. Rep.*, *37*, 118–160, doi:10.1134/S1063780X1102005X.

Zhou, X.-Z., et al. (2009), Thin current sheet in the substorm late growth phase: Modeling of THEMIS observations, *J. Geophys. Res.*, *114*, A03223, doi:10.1029/2008JA013777.

Zhou, X.-Z., D.-X. Pan, V. Angelopoulos, A. Runov, Q.-G. Zong, and Z.-Y. Pu (2016), Understanding the ion distributions near the boundaries of reconnection outflow region, *J. Geophys. Res. Space Physics*, *121*, 9400–9410, doi:10.1002/2016JA022993.

Zwickl, R. D., D. N. Baker, S. J. Bame, W. C. Feldman, J. T. Gosling, E. W. Hones Jr., D. J. McComas, B. T. Tsurutani, and J. A. Slavin (1984), Evolution of the Earth's distant magnetotail—ISEE 3 electron plasma results, *J. Geophys. Res.*, *89*, 11,007–11,012, doi:10.1029/JA089iA12p11007.